Acta Biomaterialia xxx (xxxx) xxx

Contents lists available at ScienceDirect

Acta Biomaterialia

journal homepage: www.elsevier.com/locate/actbio

Electrically conductive 3D printed $Ti_3C_2T_x$ MXene-PEG composite constructs for cardiac tissue engineering☆

Gozde Basara[a], Mortaza Saeidi-Javash[a], Xiang Ren[a], Gokhan Bahcecioglu[a], Brian C. Wyatt[b], Babak Anasori[b], Yanliang Zhang[a], Pinar Zorlutuna[a,c,*]

[a] Department of Aerospace and Mechanical Engineering, University of Notre Dame, Notre Dame, IN 46556, United States
[b] Integrated Nanosystems Development Institute and Department of Mechanical and Energy Engineering, Purdue School of Engineering and Technology, Indiana University-Purdue University Indianapolis, Indianapolis, IN, 46202, United States
[c] Department of Chemical and Biomolecular Engineering, University of Notre Dame, Notre Dame, IN 46556, United States

ARTICLE INFO

Article history:
Received 11 September 2020
Revised 30 November 2020
Accepted 15 December 2020
Available online xxx

Keywords:
$Ti_3C_2T_x$ MXene
Aerosol jet printing
Human induced pluripotent stem cell-derived cardiomyocyte
Cardiac patches
Polyethylene glycol

ABSTRACT

Tissue engineered cardiac patches have great potential as a therapeutic treatment for myocardial infarction (MI). However, for successful integration with the native tissue and proper function of the cells comprising the patch, it is crucial for these patches to mimic the ordered structure of the native extracellular matrix and the electroconductivity of the human heart. In this study, a new composite construct that can provide both conductive and topographical cues for human induced pluripotent stem cell derived cardiomyocytes (iCMs) is developed for cardiac tissue engineering applications. The constructs are fabricated by 3D printing conductive titanium carbide ($Ti_3C_2T_x$) MXene in pre-designed patterns on polyethylene glycol (PEG) hydrogels, using aerosol jet printing, at a cell-level resolution and then seeded with iCMs and cultured for one week with no signs of cytotoxicity. The results presented in this work illustrate the vital role of 3D-printed $Ti_3C_2T_x$ MXene on aligning iCMs with a significant increase in *MYH7*, *SERCA2*, and *TNNT2* expressions, and with an improved synchronous beating as well as conduction velocity. This study demonstrates that 3D printed $Ti_3C_2T_x$ MXene can potentially be used to create physiologically relevant cardiac patches for the treatment of MI.

Statement of Significance

As cardiovascular diseases and specifically myocardial infarction (MI) continue to be the leading cause of death worldwide, it is critical that new clinical interventions be developed. Tissue engineered cardiac patches have shown significant potential as clinical therapeutics to promote recovery following MI. Unfortunately, current constructs lack the ordered structure and electroconductivity of native human heart. In this study, we engineered a composite construct that can provide both conductive and topographical cues for human induced pluripotent stem cell derived cardiomyocytes. By 3D printing conductive $Ti_3C_2T_x$ MXene in pre-designed patterns on polyethylene glycol hydrogels, using aerosol jet printing, at a cell-level resolution, we developed tissue engineered patches that have the potential for providing a new clinical therapeutic to combat cardiovascular disease.

1. Introduction

Myocardial infarction (MI) is one of the most common cardiovascular diseases, which remain the leading cause of death worldwide [1,2]. MI is caused by the blockage of coronary arteries that leads to ischemia, and subsequent damage to the cardiac tissue. The damaged tissue has limited capacity to regenerate and is repaired by the resident fibroblasts and myofibroblasts, resulting in a fibrotic scar, which is no longer electrically engaged with the rest of the heart and ultimately leads to fatal arrhythmias [3,4]. In terminal situations, the therapeutic options are limited to mechanical assist devices and heart transplantation. Yet, these interventions might cause some complications such as infection and disease transmission, and in the case of transplantation, there is a

☆ Part of the Special Issue on Conductive and Electroactive Biomaterials and Bioelectronics, guest-edited by Professors Jonathan Rivnay and Mehdi Nikkhah.

* Corresponding author at: 143 Multidisciplinary Research Building, University of Notre Dame, Notre Dame, IN 46556, United States.
E-mail address: pinar.zorlutuna.1@nd.edu (P. Zorlutuna).

https://doi.org/10.1016/j.actbio.2020.12.033
1742-7061/

shortage of available donor hearts [5,6]. Hence, numerous studies have focused on developing methods to regenerate the damaged myocardium. One promising technique promoting the regeneration of the cardiac tissue is the use of engineered cardiac patches. To engineer the cardiac tissue, many different biomaterials such as collagen [7,8], albumin [9,10], gelatin methacryloyl (GelMA) [11], poly-caprolactone (PCL) [12,13], and polyglycerol sebacate [14,15] have been considered; however, their non-conductive nature can hinder the electrophysiological coupling of the cardiac patch with the host tissue [16].

Recent studies have shown that conductive polymers [17], along with composites of hydrogels or cryogels and conductive particles like carbon nanotubes (CNTs) [18–20], graphene [21,22], gold nanorods [23,24], as well as MXene nanoparticles [25] improve the electrophysiological properties of the biomaterial they were blended in, thus making them promising candidate materials for cardiac tissue engineering applications. However, clinical usage of CNTs [26,27] and gold nanorods [28] is limited due to their cytotoxicity. Similarly, graphene also may cause cytotoxicity depending on its dosage [29]. Contrarily, $Ti_3C_2T_x$ MXene, a type of two-dimensional (2D) transition metal carbides, nitrides, and carbonitrides, has many advantages including cytocompatibility, very large specific surface area, with high electroconductivity and hydrophilicity, making them suitable candidates for various biomedical applications [30–38]. As such, composites of $Ti_3C_2T_x$ MXene and hydrogels have been used as conductive biomaterials, mostly in biosensing applications [39,40].

In addition to electroconductivity, alignment of the cardiomyocytes (CMs) is also important when engineering a cardiac patch, since the functionality of the cardiac tissue is highly dependent on the linear alignment of the myofibrils and their assembly to bundles, and the longitudinal shape of the ventricular myocytes and their interconnection [41]. Hence, patterning the CMs has been the focus of several studies that aim to develop functional cardiac patches. Many of these studies have shown that the alignment of CMs enhances calcium (Ca^{2+}) handling, conduction velocity, and contractile strength. Various techniques have been used, mainly to pattern the substrates biochemically or topographically for CM alignment [42–47]. In a limited number of such studies, conductive materials were introduced alongside cell alignment cues mostly using micropatterning techniques, to achieve better mimicry of the native cardiac tissue [48–50]. However, potential applications of 3D printed conductive materials to achieve cell alignment and electroconductivity simultaneously are yet to be explored.

Aerosol jet printing (AJP) is an additive manufacturing technique, which enables the printing of nanomaterial-based inks on conformal surfaces with high resolution. The nanoink is aerosolized using an ultrasonic atomizer, then using a carrier gas (N_2) the aerosolized ink is directed to the deposition head where it is aerodynamically focused by a coaxial sheath gas flow, as shown in **Figure S1**. A variety of nanoinks with a wide range of viscosities (1–1000 cP) and nanoparticle size (as large as 500 nm) can be printed using this method [51]. AJP is particularly promising for cell patterning applications due to its high resolution, which enables printing patterns in cell-scale sizes. Moreover, its ability to print on conformal and soft surfaces, provides a significant advantage to print on hydrogels in any shape and fabricate hybrid tissue constructs.

Here, we present the first study to utilize aerosol jet printed 2D titanium carbide ($Ti_3C_2T_x$) MXene-hydrogel composites to engineer human cardiac patches. We printed $Ti_3C_2T_x$ MXene on polyethylene glycol (PEG) hydrogels using AJP method to engineer electroconductive cardiac patches that also promote alignment of the human induced pluripotent stem-cell derived cardiomyocyte (iCMs). We investigated the cytotoxicity of the $Ti_3C_2T_x$ MXene-PEG composite hydrogel on iCMs for seven days, and characterized the cardiac patches by analyzing alignment, protein expression, gene expression and Ca^{2+} flux intensity and propagation. The findings of this study suggest that $Ti_3C_2T_x$ MXene-PEG composite hydrogel is a promising electroactive scaffold for cardiac repair.

2. Materials and methods

2.1. Synthesis of $Ti_3C_2T_x$ MXene

The $Ti_3C_2T_x$ MXene ink was synthesized from 1 g of its precursor MAX phase Ti_3AlC_2 (Carbon-Ukraine Ltd, Ukraine) through selective etching of aluminum (Al) by an acidic mixture comprised of 5 wt.% hydrofluoric acid (HF), 22 wt.% hydrochloric acid (HCl), and 73% deionized (DI) water (from 48 wt.% HF stock and 37 wt.% HCl stock, Millipore Sigma, USA). The acidic mixture was added into high-density polyethylene (HDPE) container placed in an oil bath on a Corning 6795–620D Digital Stirring Hot Plate. The Ti_3AlC_2 was slowly added (3 min period), then stirred with a magnetic stir bar at 350 rpm at 35 °C for 24 h. Then, the $Ti_3C_2T_x$ solution was washed repeatedly, until the supernatant reaches a pH of 6, via centrifugation using DI water in an Eppendorf 5804R centrifuge at 3000 RCF for 3 min. After achieving a pH of 6, the $Ti_3C_2T_x$ was delaminated using 1 g of anhydrous lithium chloride (LiCl) (Millipore Sigma, USA)) in 50 mL of DI water in an HDPE container with a magnetic stir bar using an oil bath for 1 h at 1000 RPM at a temperature of 60 °C. After delamination, the solution was washed of any remaining LiCl similar to the previously described acid washing steps. Then, the delaminated $Ti_3C_2T_x$ solution was centrifuged at 2380 RCF for 1 h, and the supernatant of this cycle was used as the $Ti_3C_2T_x$ flake solution. This $Ti_3C_2T_x$ was further concentrated into ink form through centrifugation at 4000 RCF for 30 min to achieve a concentration greater than 15 mg/mL in DI water. The concentration of the supernatant was determined by vacuum-assisted filtration of 10 mL of solution, overnight drying in a vacuum oven at 100 °C, then weighing of the final free-standing $Ti_3C_2T_x$ film.

2.2. Characterization of the nanoflakes

A scanning electron microscope (SEM) (FEI Magelllan 400 XHR, USA), with working voltage 15 kV and working distance 4.5 mm was used for top-view imaging of the printed $Ti_3C_2T_x$ MXene films on glass.

2.3. Mechanical and conductive properties

Compression stiffness test was conducted by using a nanoindenter (Optics 11, USA) with an indentation probe (spring constant of 5.33 N/m, tip diameter of 50 µm. Young's modulus was calculated by determining the slope of the stress-strain plot in the elastic region, using a custom-made MATLAB code.

The conductivity measurements were performed using 2 probe method.

2.4. Cell culture

2.4.1. hiPSC culture

DiPS 1016 SevA hiPSC line derived from human skin were seeded and kept in culture on Geltrex (1% Invitrogen, USA)-coated culture flasks using mTeSR1 (StemCell Technologies, Canada) supplemented with penicillin (Pen) (VWR, USA). When hiPSCs reached a confluency of 80%, they were detached using Accutase (StemCell Technologies, Canada), and seeded in culture well plates in

mTeSR1 media supplemented with Rho-associated, coiled-coil containing protein kinase (ROCK) inhibitor (5 μM, StemCell Technologies, Canada). The culture was maintained with daily media changes until 95% confluency was reached.

2.4.2. iCM differentiation

To differentiate iCMs from hiPSCs, a previously established protocol was adapted [51]. Briefly, when the hiPSCs reached 95% confluency, they were treated with RPMI Medium 1640 (Life Technologies, USA) supplemented with B27 without insulin (2%, Invitrogen, USA), beta-mercaptoethanol (final concentration of 0.1 mM, Promega, USA) and Pen (1%) (CM (-)) with the addition of Wnt activator, CHIR99021 (CHIR) (12 μM, Stemgent, USA). Precisely twenty-four hours later, media were replaced with CM (-) without CHIR. On day 4, iCMs were treated with CM (-) media with the addition of Wnt inhibitor IWP-4 (5 μM, Stemgent, USA). On day 6, media were changed back to only CM (-). Three days later (day 9), media were replaced with RPMI Medium 1640 supplemented with B27 (2%, Invitrogen, USA), beta-mercaptoethanol (final concentration of 0.1 mM, Promega, USA), and Pen (1%) (CM (+)). After day 9, media were changed every 3 days, and beating was observed generally by day 21 of differentiation as stated in previous papers [52–54].

2.5. Preparation of cardiac patches

The pre-hydrogel solution was prepared by dissolving PEG (diacrylate, 3.5 kDa, 10% *w/v*, JenKEM, USA) in phosphate-buffered saline (PBS) (VWR, USA) and adding photoinitiator (PI) (0.1% *w/v* in PBS) (Irgacure 2959, Sigma-Aldrich, USA). To dissolve PEG in PBS, the solution was mixed thoroughly using a vortex. By using a pipette, 30 μl of PEG solution was placed in a disk-shaped polydimethylsiloxane (PDMS) mold (diameter: 8 mm, thickness: 0.5 mm) placed onto a glass cover slip in a 24-well plate. The solution was then exposed to UV radiation at 6.9 mW/cm^2 by using a UV lamp (Lumen Dynamics, Mississauga, ON, Canada). After gelation, the molds were removed carefully. As a result, disk-shaped hydrogel slabs were obtained. The hydrogels were washed three times for 5 min each in PBS, and immediately placed in 37 °C.

High resolution AJP was used for printing various patterns including straight line, bowtie, Hilbert's curve, and square (1 mm^2) on the PEG hydrogels or glass cover slips. The printing process is non-contact and conformal, allowing patterning over conformal surfaces. During the AJP process, the nanoink was atomized into droplets ranging from 1 to 5 μm in diameter using an ultrasonic atomizer. Prior to printing $Ti_3C_2T_x$ MXene, to assure there was no contamination, all the printer parts including the deposition head, ink reservoir, connecting tubes and nozzle were cleaned by sonication in a special solution (Branson, MC-3 cleaner solution) for 3 h. Additionally, before placing glass substrates containing PEG hydrogels, the printer platen was cleaned with isopropyl alcohol followed by DI water for 5 min. In order to achieve a high-quality print, several printing parameters, such as the flow rate of the carrier gas, the flow rate of the sheath gas that collimates the aerosol flow into a narrow beam, ultrasonic atomizer power, platen speed and nozzle size, were optimized. **Figure S2** demonstrates the print quality before and after optimizing the printing parameters and the optimized printing parameters are presented in **Table S1**. All the patterns were printed using a nozzle with 100 μm diameter to acquire the desired resolution and $Ti_3C_2T_x$ was printed with a single pass with ~1 μm thickness (**Figure S3**).

Immediately after printing, the $Ti_3C_2T_x$ MXene-PEG composite hydrogels were sterilized under UV for 30 min. After sterilization, fibronectin in PBS (50 μg/mL, Sigma-Aldrich, USA) was placed on the gels and they were placed at 37 °C for 30 min. The iCMs were detached using trypsin-EDTA (0.25%, Corning, USA) and re-suspended in Dulbecco's Modified Eagle Medium (Hyclone, USA, DMEM) supplemented with fetal bovine serum (10%, Hyclone, USA, FBS) and Pen (1%). The fibronectin solution was then removed, and the cells were seeded at a density of 5×10^5 cells/ml. The next day, media were replaced with CM (+) media.

2.6. Transmission electron microscopy (TEM) imaging

$Ti_3C_2T_x$ MXene-PEG constructs were fixed in 2% glutaraldehyde (Sigma-Aldrich, USA) in 0.1 M cacodylate buffer (Electron Microscopy Sciences, USA) for 2 h. Then post fixation was performed in 1% Osmium tetroxide (Electron Microscopy Sciences, USA) in the same buffer for one hour. They were then dehydrated in a graded series of ethanol. For infiltration, the samples were kept in a mixture of 100% ethanol and Spurr's low viscosity embedding media (Sigma-Aldrich, USA) (1:1 overnight, then 1:3 for 8 h and 1:3 for 8 h) before replaced with 100% Spurr's media. The next day, the constructs were placed in embedding BEEM capsules (Electron Microscopy Sciences, USA), then the capsules were filled with Spurr's low viscosity embedding media and placed into 70 °C oven to polymerize overnight. Using a Leica UC7 Ultramicrotome and a Diatome diamond knife, 70 nm thick sections were obtained.

To perform TEM imaging of $Ti_3C_2T_x$ MXene, drop casting method was used. After diluting $Ti_3C_2T_x$ MXene with DI water, a droplet of the diluted solution was placed on the TEM grid and left for air drying. The samples then imaged using a JEOL 2011 electron microscope equipped with AMT CCD camera at 120 kV.

2.7. Live dead assay

Cardiac patches were prepared as described in the previous section. Three different patterns were printed on PEG gels: straight line, bowtie, and Hilbert's curve. To evaluate the cytotoxicity of $Ti_3C_2T_x$ MXene, live/dead assay (Life Technologies, USA) was performed on day 2 after seeding the $Ti_3C_2T_x$ MXene-PEG composite hydrogels ($n = 3$, for each condition), following the manufacturer's instructions. Briefly, the constructs were washed and incubated for 30 min in a solution containing Calcein AM (live cells, green, 2 μM) and Ethidium homodimer-1 (dead cells, red, 4 μM). The images were taken using a fluorescence microscope (Zeiss, Hamamatsu ORCA flash 4.0, Thornwood, NY, USA). For Hilbert's curve pattern, live/dead assay was additionally performed on days 4 and 7, following the same protocol described above. To be able to image the cells attached on $Ti_3C_2T_x$ MXene, the constructs attached on glass coverslips were transferred up-side down to a glass-bottom dish. The images were analyzed using in house MATLAB code and the live cell percentage was calculated by using Eq. (1).

$$\text{Livecell}(\%) = [(\text{livecellnumber})/(\text{totalcellnumber})] * 100 \quad (1)$$

2.8. Immunostaining

For immunostaining three different conditions were used: MXene printed on glass with a pattern, 1mm^2 $Ti_3C_2T_x$ MXene squares printed on PEG (unpatterned), and printed $Ti_3C_2T_x$ MXene on PEG with Hilbert's curve (patterned). Right after printing and sterilizing, cells were seeded on the constructs as described previously and were maintained in culture for a week with media changes every 2 days. After seven days in culture, constructs were washed with PBS (Corning, USA) and fixed using paraformaldehyde (4%, Electron Microscopy Sciences, USA) for 15 min at room temperature. After fixing, they were washed with PBS and then permeabilized in Triton X-100 (0.1%, Sigma-Aldrich, USA) for 30 min. They were washed with PBS and blocked using goat serum (10%, Sigma-Aldrich, USA)

for 1 h. After blocking, constructs were incubated with sarcomeric alpha actinin (ab9465, Abcam, United Kingdom), and Connexin 43 (CX43) (ab11370, Abcam, United Kingdom) primary antibodies diluted (1:200) and (1:100) respectively in goat serum at 4 °C overnight. The next day, the constructs were washed thoroughly with PBS and then incubated with Alexa Fluor 647 (A21245, Life Technologies, USA) and Alexa Fluor 488 (A11001, Life Technologies, USA) diluted (1:200) in goat serum at 4 °C for 6 h. After incubation, constructs were washed with PBS until no background was seen. The samples were then mounted using a mounting medium with DAPI (ab 104139, Abcam, United Kingdom). Imaging was then performed using a fluorescence microscope (Zeiss, Hamamatsu ORCA flash 4.0, Thornwood, NY, USA). Sarcomere lengths and orientations, and CX43 expressions were measured using NIH ImageJ software.

2.9. Quantitative real time pcr (qRT-PCR)

To observe the effect of MXene and patterning separately, three different sample types were prepared: (i) iCMs seeded on glass only, (ii) 1 mm^2 $Ti_3C_2T_x$ MXene squares printed on PEG (unpatterned), and (iii) Hilbert's curve-patterned $Ti_3C_2T_x$ MXene printed on PEG (patterned). After one week in culture, RNA was collected using a total RNA isolation kit (RNeasy, Qiagen, USA). The purity and concentration of RNA were measured using a NanoDrop 2000 Spectrophotometer (Thermo Fisher Scientific, USA). Using the iScript cDNA Synthesis Kit (Bio-Rad, USA), RNA was converted into cDNA. Certified human gene-specific primers were purchased from Bio-Rad (**Table S2**). For qRT-PCR reactions, iTaq SYBR Green Supermix (Bio-Rad, USA) was used and the reactions were run on CFX Connect 96 Real Time PCR system (Bio-Rad, USA) in duplicates. To quantify the relative expression of genes, $\Delta\Delta$Ct method was applied using GAPDH as the housekeeping gene.

2.10. Western blotting

The cardiac patches were cultured for a week. At day 7, the cell lysates were collected using RIPA buffer (ab156034, Abcam, United Kingdom) with protease inhibitor (Calbiochem, USA) and ran on 8% SDS-PAGE gel (Bio-Rad, USA). Then proteins were transferred to PVDF membrane (Bio-Rad, USA). Immunoblotting was performed using antibodies specific to TNNT2 (ab209813, Abcam, UK), MYH7 (HPA001239, Sigma-Aldrich, USA), Connexin 43 (3512S, Cell Signaling Technology, USA), SERCA2 (9580S, Cell Signaling Technology, USA), and beta-actin (ab8226, Abcam, UK), followed by secondary antibody staining (ab205718, Abcam, UK). Using chemiluminescence detection, the antibody-bound proteins were imaged. Quantification of protein expression levels were performed using NIH ImageJ software.

2.11. Ca^{2+} flux assay

The contraction kinetics of the iCMs were assessed by investigating Ca^{2+} transient kinetics by labeling them using a Ca^{2+}-sensitive dye and observing Ca^{2+} handling during the spontaneous beating. Briefly, at day 7 of culture, the media were removed, and the constructs were washed with PBS. They were then incubated with Fluo-4 AM (Thermo Fischer Scientific, USA) prepared following manufacturer's instructions at 37 °C for 30 mins. The solution was then replaced with warm CM (+) media and immediately after real time imaging was performed using a fluorescence microscope (Axio Observer. Z1, Zeiss, Hamamatsu C11440 digital camera) at 200 ms exposure for 30 s. The videos were analyzed using a customized MATLAB code. Briefly, the colors of the videos were split into red, green, and blue channels. The green compartment on each frame was used to identify the beating of the cardiac cells and the green intensities were normalized using the red compartment of the images. Using the intensity profile, time to peak, 50% decay time and 90% decay time were calculated with a slight deviation, where the maximum intensity point was identified as the peak. For fluorescence decay occurred within 200 ms, the decay points were estimated by linear fitting between the peak and the baseline. The peaks were plotted together by coinciding with the beating starting points. The fitting of each beating peak was represented by a dashed line, and the average of the fitting curves was represented by a solid line.

To measure the conduction velocity, the center of beating for each group was identified and marked with a yellow dot. Using a customized MATLAB code, the travel duration of Ca^{2+} flow between two adjacent points was calculated. All the dimensions were calculated using NIH ImageJ software. Then the conduction velocity was simply calculated as the ratio of the distance over time of travel.

2.12. Statistical analysis

For all replicates except for western blotting, the mean ± standard deviation (SD) was reported. For western blotting standard error of the mean was reported. To find any statistically significant differences, one-way analysis of variance (ANOVA) followed by Tukey's post hoc was used and $p<0.05$ was considered statistically significant.

3. Results

3.1. Preparation of $Ti_3C_2T_x$ MXene-PEG composite hydrogels

Three different patterns were printed on PEG hydrogels: straight line, bowtie and Hilbert's curve. The straight line was chosen to achieve the linear alignment of iCMs. In addition to their iCM alignment ability, bowtie and Hilbert's curve patterns were chosen for their specific features. The bowtie geometry was chosen because it is stiffer in one direction than the other, like the native heart [55]. Hilbert's curve was chosen since it is a self-similar structure and a space-filling curve, which is a continuous path that never crosses itself [56]. This property is important for tracking Ca^{2+} signal propagation as the iCMs contract which is explained further in the electrophysiological characterization section.

The preparation steps of $Ti_3C_2T_x$ MXene-PEG composite hydrogels are shown in Fig. 1. $Ti_3C_2T_x$ MXene nanosheets were prepared by selective etching of Al layers from Ti_3AlC_2 MAX powder with HF/HCl acidic combination (Fig. 1**a**). The schematic of the AJP process of $Ti_3C_2T_x$ MXene patterns on PEG hydrogel is shown in Fig. 1**b**. Different patterns were printed on PEG hydrogels (Fig. 1**c**). A top view SEM image of deposited $Ti_3C_2T_x$ MXene shows the restacked nanoflakes after deposition, which have lateral sizes within 1 µm range (Fig. 1**d**). To observe the ultrastructure of $Ti_3C_2T_x$ MXene and $Ti_3C_2T_x$ MXene-PEG composite hydrogels TEM imaging was performed (Fig. 1**e** and 1**f**). The results confirmed the restacked nanoflakes structure seen in SEM image when printed on PEG (Fig. 1**f**) compared to more distributed nanoflakes and visible structure of $Ti_3C_2T_x$ MXene when drop casted (Fig. 1**e**).

3.2. iCMs alignment and viability on $Ti_3C_2T_x$ MXXene-PEG composite hydrogels

Using AJP, $Ti_3C_2T_x$ MXene was successfully printed on glass, GelMA and PEG hydrogels. After seeding the iCMs on these constructs, cell attachment and alignment were characterized **(Figure S4)**. Superior alignment of the iCMs was observed on the $Ti_3C_2T_x$ MXene-PEG hydrogels; therefore, PEG hydrogels were chosen for

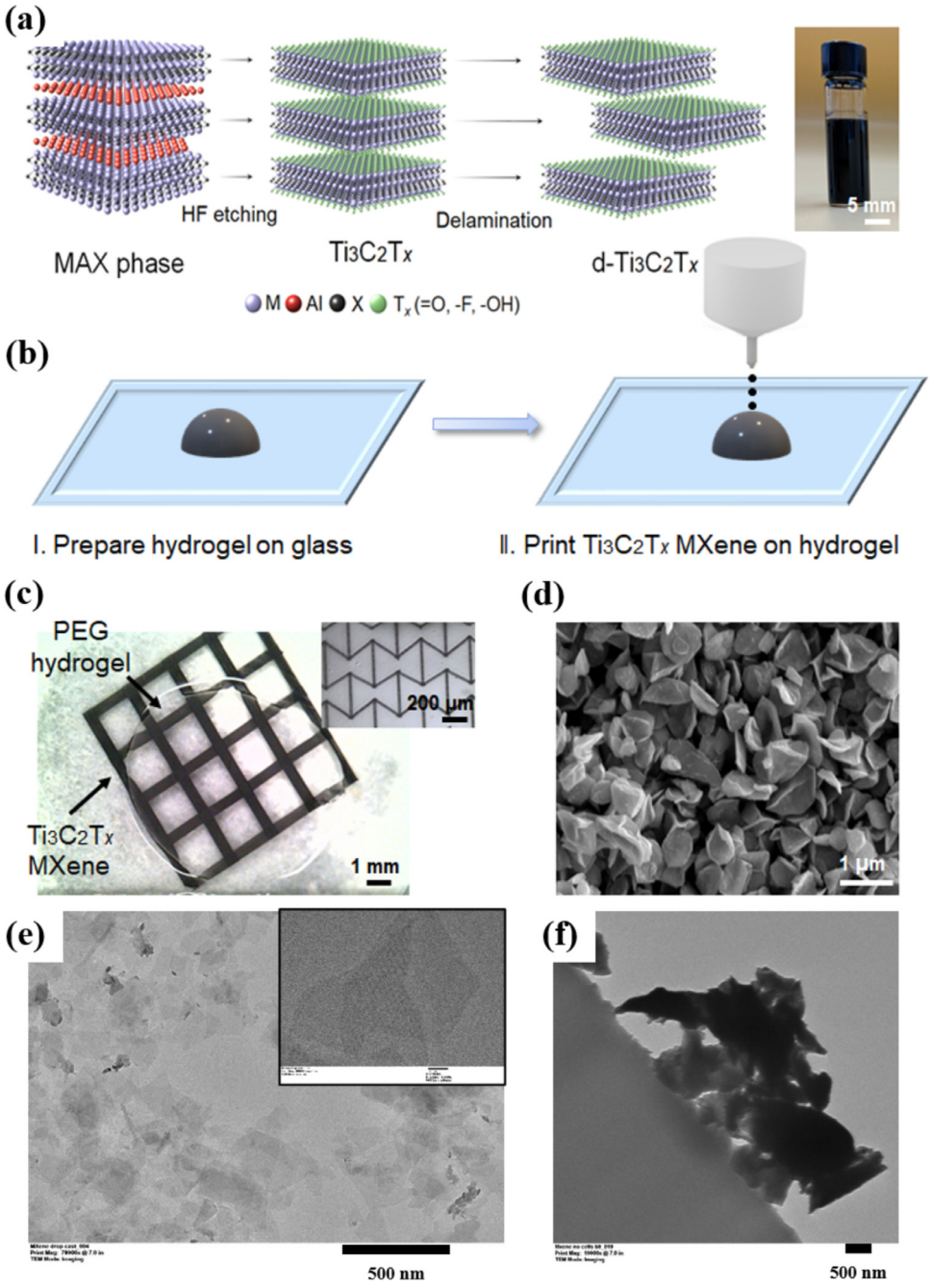

Fig. 1. 3D conformal aerosol jet printing of $Ti_3C_2T_x$ MXene on polyethylene glycol (PEG) gels. (a) Scheme illustrations of selective hydrofluoric acid (HF) etching of layers of Ti_3AlC_2 MAX phases for the preparation of $Ti_3C_2T_x$ MXene. (b) Schematic illustration of printing $Ti_3C_2T_x$ MXene-hydrogel composite using aerosol jet printer including (I) preparing PEG hydrogel on glass substrate, (II) printing $Ti_3C_2T_x$ MXene on hydrogel. (c) Printed $Ti_3C_2T_x$ MXene on PEG hydrogel with a square (81 mm^2) pattern. The inset is printed bowtie pattern $Ti_3C_2T_x$ on PEG. (d) Top view SEM image of printed $Ti_3C_2T_x$ MXene nanoflakes. (e) TEM image of $Ti_3C_2T_x$ MXene. (f) TEM image of $Ti_3C_2T_x$ MXene printed on PEG hydrogel.

further investigation. When the composite constructs were prepared using PEG hydrogels, cells attached only on $Ti_3C_2T_x$ MXene, resulting in the patterning of the iCMs (Fig. 2**a-c**). Cell viability on day 2 of culture was over 85% (89% ± 8% for lines, 94% ± 3% for bowtie, and 85% ± 6% for Hilbert's curve) in all patterns. Hilbert's curve was chosen to study the effect of $Ti_3C_2T_x$ MXene patterning on protein and gene expressions and the beating properties of the iCMs, because it enabled tracking of Ca^{2+} signal propagation. Cell viability of the Hilbert's curve-patterned MXene-PEG composite hydrogels was further assessed on days 4 and 7 of culture (Fig. 2**d**). The percentage of live cells increased over time, from 85% ± 6% on day 2 to 89% ± 7.0% on day 4, and 93% ± 1% on day 7 (Fig. 2**e**), indicating that MXene was compatible with the iCMs.

3.3. Phenotypical characterization of iCMs on $Ti_3C_2T_x$ MXene-PEG composite hydrogels

To assess the effect of $Ti_3C_2T_x$ MXene on the structure and function of the iCMs, cells were seeded on the straight line-patterned $Ti_3C_2T_x$ MXene printed on glass, unpatterned square shaped $Ti_3C_2T_x$ MXene (1mm^2) printed on PEG, and Hilbert's curve-patterned $Ti_3C_2T_x$ MXene printed on PEG (Fig. 3). Cells

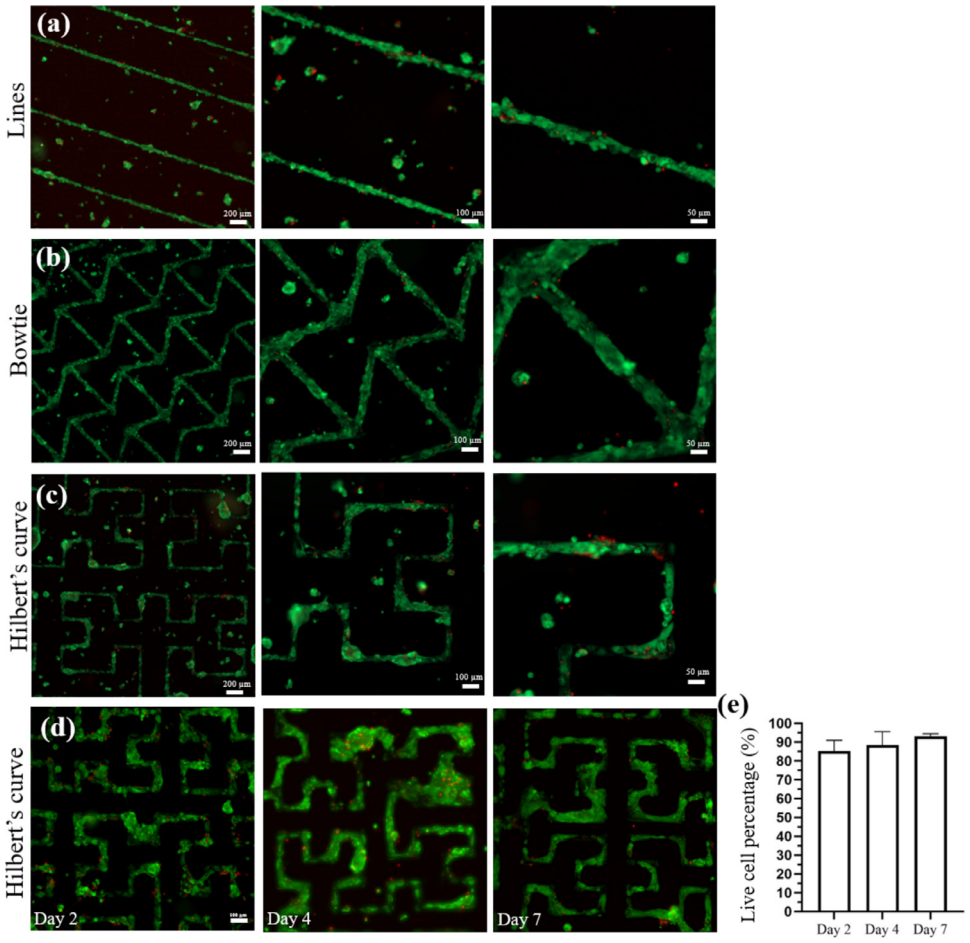

Fig. 2. Patterning and viability analysis of iCMs on $Ti_3C_2T_x$ MXene-PEG hydrogel composite. (a) Straight lines, (b) Bowtie, (c) Hilbert's curve, (d) iCM viability analysis on Hilbert's curve pattern on days 2, 4 and 7, (e) live cell percentage at the corresponding days.

seeded on the straight line-patterned MXene on glass samples preferentially attached on the glass and did not align along the lines. On day 7 of incubation, expression of CX43, the inter-cellular junction protein, and sarcomeric alpha-actinin, the cytoskeletal actin binding protein, was assessed by immunostaining **(**Fig. 3**a-c).** All groups showed some CX43 expression (Fig. 3**a**) and striated and aligned sarcomeric alpha-actinin structures (Fig. 3**b**). The average sarcomere lengths were measured to be 1.9 ± 0.2 µm, 1.8 ± 0.2 µm, and 1.6 ± 0.3 µm for the straight line-patterned $Ti_3C_2T_x$ MXene printed on glass, unpatterned $Ti_3C_2T_x$ MXene-on-PEG, and patterned MXene-on-PEG, respectively (Fig. 3**d**), which were all significantly different from each other. Directionality analysis showed that sarcomeres were better aligned on the patterned $Ti_3C_2T_x$ MXene-on-PEG (standard deviation: 15.9°) than on glass (standard deviation: 34.9°) (Fig. 3**e**). Additionally, the sarcomeres were oriented almost in the same direction with the $Ti_3C_2T_x$ MXene pattern (6.3° ± 15.9° difference between the sarcomeres and the struts), while on glass they diverged from the strut direction (41.5° ± 34.9° difference between the sarcomeres and the struts). To assess the effect of $Ti_3C_2T_x$ MXene and patterning on the cardiac maturity related gene expression, qRT-PCR was performed on day 7 of culture. *MYH7* expression increased significantly in the presence of $Ti_3C_2T_x$ MXene (1.4 ± 0.1 fold increase) and with patterning (2.3 ± 0.1 fold increase) (Fig. 3**f**). Similarly, a significant increase in *TNNT2* expression was observed in the unpatterned (1.6 ± 0.1 fold) and patterned $Ti_3C_2T_x$ MXene (2.1 ± 0.1 fold) compared to glass control, indicating improved iCMs maturity. For *SERCA2*, even though no significant difference was observed between the unpatterned $Ti_3C_2T_x$ MXene and glass control (1.2 ± 0.3 fold increase), patterning of $Ti_3C_2T_x$ MXene increased the expression significantly (1.7 ± 0.1 fold) compared to the glass control. In the presence of $Ti_3C_2T_x$ MXene, *GJA1* (Connexin 43) increased significantly (1.2 ± 0.1 fold) compared to the on-glass controls. However, no significant difference was observed between the patterned and control groups (1.0 fold change). Western blotting showed no significant difference between the glass control, unpatterned and patterned $Ti_3C_2T_x$ MXene for the MYH7, SERCA2, Connexin 43 and TNNT2 protein expressions (Fig. 3**g,h**).

3.4. Electrophysiological characterization of the engineered cardiac patches

To investigate the contraction kinetics of the engineered cardiac patches, the changes in their Ca^{2+} transient kinetics were investigated. At day 7 of culture, the patches were monitored in real-time for the Ca^{2+} handling ability of iCMs as they beat spontaneously. Maximum fluorescence intensity was observed at peak flux (Fig. 4**a**). The beating profile of cells on glass was plotted using the change in intensity over time (30 s) (Figs. 4**b** and **c**). Then, using the beating profile, time to peak flux, 50% decay time and 90% decay time values were calculated as 300.0 ± 109.5 ms, 441.0 ± 103.0 ms and 688.5 ± 94.6 ms, respectively (Fig. 4**d**). The beat rate was measured to be 12 bpm. To track the Ca^{2+} flow in the patterned cardiac patches, the imaged area was divided into

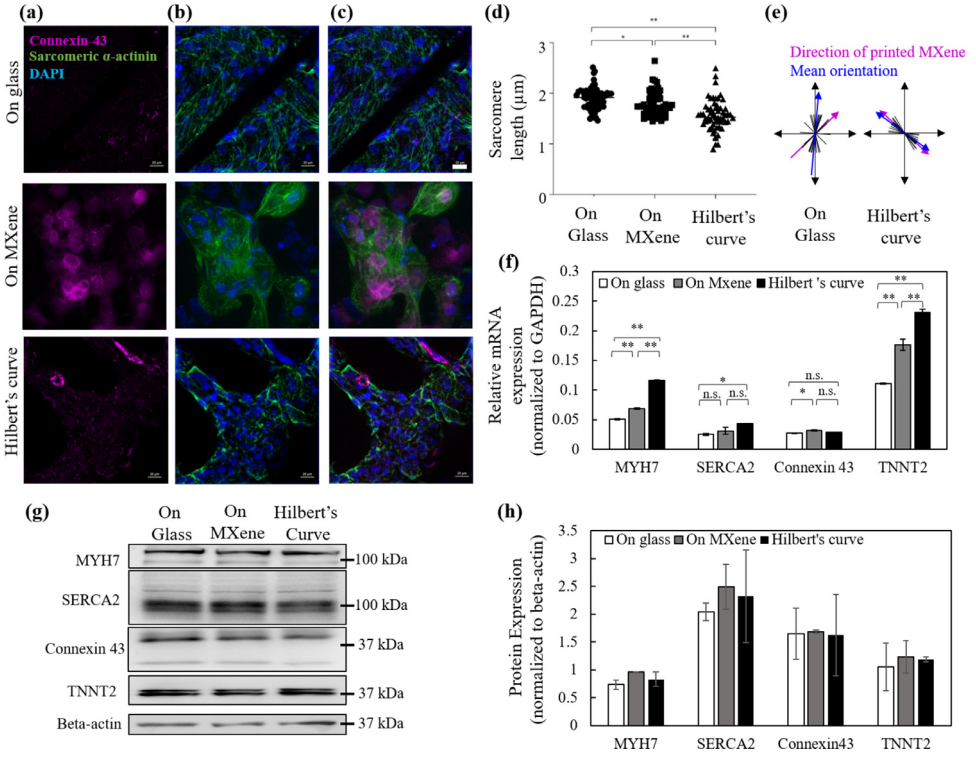

Fig. 3. Immunostaining characterization and qRT-PCR analysis of iCMs at day 7 (All scale bars indicate 20 μm). (a) The CX-43 staining of the straight line-patterned $Ti_3C_2T_x$ MXene printed on glass controls, on unpatterned $Ti_3C_2T_x$ MXene controls, and Hilbert's curve-patterned $Ti_3C_2T_x$ MXene printed on PEG. (b) The sarcomeric alpha-actinin staining of on-glass controls, on-$Ti_3C_2T_x$ *MXene* controls and Hilbert's curve. Cell nuclei are stained with DAPI (blue). (c) Combined Connexin-43 and sarcomeric alpha-actinin staining of on-glass controls, on- $Ti_3C_2T_x$ MXene controls and Hilbert's curve. Cell nuclei are stained with DAPI (blue). (d) Sarcomere length quantification in μm (* represents $p < 0.05$ and ** represents $p < 0.01$). (e) Directionality analysis. (f) qRT-PCR analysis of relative mRNA expression of cardiac markers *MYH7, SERCA2, GJA1,* and *TNNT2* (** represents $p<0.01$ and n.s. represents non-significant) (g) Western blotting for the expressions of MYH7, SERCA2, GJA1, and TNNT2 proteins. (h) Quantification for the western blotting ($n = 2$). (For interpretation of the references to colour in this figure legend, the reader is referred to the web version of this article.)

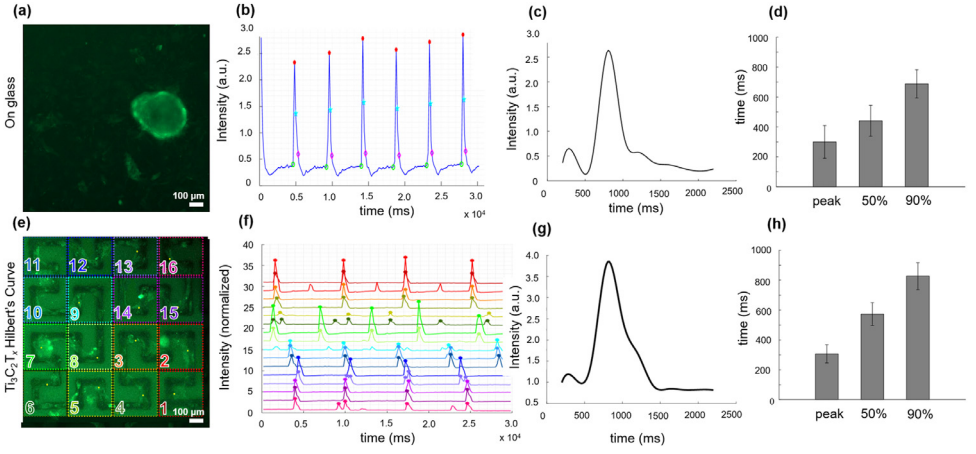

Fig. 4. Characterization of the spontaneous beating of iCMs when seeded on glass (a to d) and on patterned $Ti_3C_2T_x$ MXene-PEG composite hydrogel (e to h). (a) A representative snap shot from calcium flux time-lapse recording, (b) Beating profile as extracted from these time-lapse recordings. (c) Intensity of calcium flux time-lapse image and (d) Calculated time to peak intensity, 50% decay time from peak, and 90% decay time from peak. (e) A representative snap shot from calcium flux time-lapse recording of patterned $Ti_3C_2T_x$ MXene-PEG composite hydrogel (the pattern was divided into 16 groups and each group was represented with a different color). (f) Beating profile of each designated group as extracted from these time-lapse recordings. The color of the profiles follow the colors of the sub-regions in panel e. (g) Average intensity of calcium flux time-lapse image. (h) Calculated average time to peak intensity, 50% decay from peak, and 90% decay from peak.

sixteen sub-regions (Fig. 4**e**). Beating profiles were plotted separately for each sub-region (Figs. 4**f** and **g**). Similar to the on-glass controls, time to peak, 50% decay time and 90% decay time values were calculated for each sub-region and the average was calculated as 306.9 ± 60.6 ms, 573.0 ± 76.5 ms and 826.9 ± 90.2 ms, respectively (Fig. 4**h**). The beat rates ranged from 8 to 14 bpm. The percentage of the beating cell area was much greater on the Hilbert's curve patterned $Ti_3C_2T_x$ MXene on PEG (82%) than on the glass control (36%) (**Movie S1**). To further assess the effect of patterned $Ti_3C_2T_x$ MXene on the contraction kinetics of the iCMs, the conduction velocity of iCMs was measured by simply tracing the Ca^{2+} signal between the adjacent groups (Fig. 4**e** and **Movie S2**). It was observed that some groups, such as 1 and 2, 2 and 3, and 7 and 8, beat almost simultaneously. The conduction velocity between

these groups were calculated as 4.3 cm/s, 6.5 cm/s and 5.1 cm/s, respectively. On the other hand, the conduction was detectable visually between some other groups, such as 3 and 4, and 9 and 10, for which the conduction velocity was measured as 0.5 cm/s and 0.3 cm/s, respectively.

4. Discussion

Engineered cardiac patches are promising candidates for the treatment of infarcted cardiac region after MI, by promoting the regeneration of the cardiac tissue. There are a number of studies that have investigated the applications of several different conductive materials for fabricating cardiac patches [18,19,21,22,24,25,57]. However, the potential of 2D $Ti_3C_2T_x$ MXene nanoflakes and MXene/hydrogel composites is yet to be fully explored. In a recent study, Ye and colleagues obtained conductive nanocomposite hydrogels by synthesizing titanium carbide MXene (Ti_2CT_x)-cryogels through mixing polyethylene glycol diacrylate (PEGDA), a crosslinker solution and Ti_2CT_x solid particles dispersed in water, and seeded these gels with rat cardiomyocytes to engineer cardiac patches [25]. Here, in this study, rather than simply embedding the $Ti_3C_2T_x$ MXene nanoparticles in the hydrogel, we deposited the 2D MXene nanoflakes on a hydrogel base using AJP, thus achieving continuous filaments with which we aimed to enable cell alignment while enhancing the conductivity. By seeding iCMs on the composite constructs, we were able to demonstrate the cell alignment with great viability. Although there are studies that combined electroconductivity and fibrillar structure of the native heart [48–50], none of them except one used 3D printing. In a recent study, extrusion printing, which has a resolution of couple hundred micrometers, was used to fabricate a hydrogel with gold nano rods and cell mixture where an external electrical field was used to help align the nano rods and thus the cells [58]. In another recent study the potential application of Ti_3C_2 MXene blended within hyaluronic acid-alginate hydrogels as a bioink for extrusion based 3D printing was investigated using Human Embryonic Kidney 293 (HEK-293) cells [59]. Our study advances the field by introducing cell-level resolution for printing (which requires a high sheath flow and an optimization process for the printing parameters) a cell-friendly conductive material directly on a 3D conformal scaffold using AJP. Moreover, compared to other traditional fabrication methods such as infusion molding, AJP allows for fabricating the materials in desired shapes without the requirement of product specific molds and in a faster manner.

As the hydrogel part of the composite construct, we chose PEG (diacrylate, 3.5 kDa) due to its low protein adsorption properties [60] allowing the cell attachment on MXene alone, thus enabling the patterning of the iCMs. We printed 2D $Ti_3C_2T_x$ MXene nanoflakes on PEG hydrogels in different patterns to show that cells can be patterned in various shapes. We reported high cell viability for each pattern. However, we observed that the straight-line patterns fell apart more easily during longer culture periods. Additionally, we considered Hilbert's curve pattern to be more suitable for investigating Ca^{2+} transient kinetics of the iCMs and calculating their conduction velocity because of its continuous and non-self-intersecting property. We reported high viability of iCMs when they were seeded on patterned $Ti_3C_2T_x$ MXene-PEG hydrogels and kept in culture for a week, indicating that $Ti_3C_2T_x$ MXene is not cytotoxic. Previous studies reported similar results where no negative effect was observed for $Ti_3C_2T_x$ MXene on the neuron and muscle activity of the zebrafish embryo model [61], rat CMs [25], and neurons [62].

To observe the effect of $Ti_3C_2T_x$ MXene and patterning on iCM phenotype and maturity, we performed immunostaining, qRT-PCR and western blotting. In this study, we only investigated the effect of Hilbert's curve pattern, but a future study may be dedicated to studying the effect of different patterns on iCM function. Immunostaining results revealed that CX43 was mainly localized to the cell membrane and its expression was greatly increased in the presence of $Ti_3C_2T_x$ MXene and patterning (Fig. 3a). CX43 is a well-known gap junction protein expressed between CMs and plays an important role in synchronous contraction by regulating electrical impulse propagation [25]. Hence, improved levels of CX43 expression located mostly between the cell boundaries indicate better coordination of the iCM network. Similarly, in the literature, this trend has been reported for other electroconductive scaffolds, including hydroxyethyl methacrylate embedded with gold nanoparticles, nanocomposites consisting of alginate and nanowires, and decellularized cardiac ECM blended with polypyrrole [63–65]. Structural organization and expression were investigated by staining the structural maturity marker, sarcomeric alpha actinin and measuring the sarcomere length and direction. Measured values were in the same range with other studies that have been done with human or mouse-derived CMs [66,67], but slightly lower than the sarcomere length of human adult CMs, which was reported to be over 2 μm [68]. We observed larger sarcomere length of iCMs when they were seeded on the cover glass compared to when seeded on unpatterned and patterned $Ti_3C_2T_x$ MXene-PEG hydrogels. It has been shown that stiffer substrates enhance sarcomere length [69]. Therefore, this increase can be explained with the greater elastic modulus of the cover glass, which is in GPa range [70], compared to the underlaying PEG hydrogel, whose elastic modulus is measured as 7.0 kPa $\pm$ 1.6 kPa using a nano-indenter. Similarly, the elastic modulus of the patterned and unpatterned $Ti_3C_2T_x$ MXene measured to be 17.5 kPa $\pm$ 5.5 kPa and 144.5 kPa $\pm$ 38.8 kPa, respectively. Since the patterned MXene contains less $Ti_3C_2T_x$ than the unpatterned one, it is relatively softer and has a similar elastic modulus with the healthy heart tissue [71]. Although glass cover slip increases the sarcomere length, it is not a physiologically relevant material due to its 3 orders of magnitude higher elastic modulus compared to the native cardiac tissue [72]. Moreover, even though the sarcomere length was slightly smaller when iCMs were seeded on the patterned $Ti_3C_2T_x$ MXene-PEG hydrogel constructs, we observed that the sarcomere orientation was in line with the printed pattern orientation. This observation is valuable because the linear alignment of iCMs improves cardiac function [41]. Additionally, it has been shown that myofibril alignment not only results in higher contractile force but also in more efficient translation of sarcomere shortening (the difference between the sarcomere length at the relaxed and contracted states) to contractile output in iCMs [73].

Besides alignment and sarcomere length, sarcomeric isoform switching is an essential element of myofibril maturation, and *MYH7* is the predominant isoform in the adult human heart [74]. Our results showed a significant increase in *MYH7* in the presence of $Ti_3C_2T_x$ MXene and with patterning. Overall, even though the sarcomere length slightly decreased when iCMs were cultured on MXene, better myofibril alignment and increased expression of *MYH7* indicate improved contractility and maturity.

In addition to *MYH7*, other maturation marker expressions in mRNA level was investigated using qRT-PCR. We selected genes that are known to upregulate with the increasing CM maturity level such as *TNNT2, SERCA2* and *GJA1* [57,72,75,76]. We observed a significant increase in *TNNT2* expression indicating the improved maturity in the presence of $Ti_3C_2T_x$ MXene and patterning, which is consistent with the previous reports [19,72,77]. We also reported an increased expression of *SERCA2,* which is an indication of improved Ca^{2+} handling properties, since *SERCA2* was shown to play a critical role in excitation/contraction coupling of CMs [66,72] and it increases with maturity [74]. Even though no change in *GJA1* expression was observed, this might be an indication that transcription has equilibrated itself to a similar level as the on-glass control

turnover levels, but with a higher total amount of CX43 expression, which was verified by the immunostaining results. Western blot analysis for protein expressions such as MYH7, SERCA2, Connexin 43 and TNNT2 revealed no significant effect of $Ti_3C_2T_x$ MXene or patterning, although a trend of increase can be seen (Fig. 3**h**). Even though a significant increase in *MYH7*, *SERCA2*, and *TNNT2* gene expression in the presence of unpatterned and patterned $Ti_3C_2T_x$ MXene was observed, these were likely not translated to protein expression results in the duration of this study. Longer culture times might be necessary to see the effect of the gene upregulations at the protein level.

In addition to phenotypical characterization of the cardiac patches, we reported a characterization of contraction kinetics by examining the Ca^{2+} handling and conduction velocity. Although, we observed a similar contraction duration for on-glass controls and for the patterned $Ti_3C_2T_x$ MXene-PEG hydrogel; the 50% and 90% decay durations were prolonged for the latter. Previous reports related to this prolonged duration with maturity [66,72,77]. In contrast to previous reports where the conductive material improved the beating rate of the rat CMs [18,21], our results show no significant improvement in the beating rate of the iCMs in the presence of MXene. However, we observed that $Ti_3C_2T_x$ MXene significantly increased the beating cell area percentage.

When the conduction velocity between the groups was measured, we observed a slight difference between them which can be explained with the minor changes in the degree of iCMs attachment on the different sections of the MXene pattern resulting in slightly uneven cell densities throughout the large pattern. In their study, Ellis et al. measured the conduction velocity of reseeded iCMs to be 4.6 cm/s using a microelectrode array (MEA), for which the conduction velocity is defined as the field potential propagation velocity across the MEA surface [54,78]. After the surface area of Hilbert's curve pattern was normalized to the MEA's, the conduction velocities calculated in this study were either similar or slightly better than the previous reports. This increase in the conduction velocity of the iCMs could conceivably be an outcome of the conductive property of the $Ti_3C_2T_x$ MXene which was measured as 1.1×10^4 S/m when printed on PEG and greatly improved the conductivity of PEG (0.1 S/m).

Overall, in this study we investigated the potential of the 2D $Ti_3C_2T_x$ MXene material for cardiac patch applications. In light of our results, we conclude that 3D printed $Ti_3C_2T_x$ MXene is a promising technique for engineering cardiac patches. By integrating 2D $Ti_3C_2T_x$ MXene nanoflakes into nonconductive hydrogels the synchronous beating of the iCMs could be improved. Furthermore, the conductive properties of the composite hydrogel could improve the electrophysiological coupling of the patch with the infarcted region. By using the patterning capability of this material and the printing method we used, the cells on the patch can be made in the same orientation with the rest of the heart, which would result in additional improvements in the signal transfer from the healthy heart tissue through the patch.

Declaration of Competing Interest

The authors declare that they have no known competing financial interests or personal relationships that could have appeared to influence the work reported in this paper.

Acknowledgements

This work was supported by NIH Award #1 R01 HL141909–01A1 and NSF-CAREER Award # 1651385. Y.Z would like to acknowledge funding support from the National Science Foundation under award CMMI-1747685. We thank Dr. Bowen Zhang for his contribution in $Ti_3C_2T_x$ MXene preparation. We thank Dr. Yury Gogotsi for his scientific input and guidance. We thank Sarah Chapman for her help with sample preparation for TEM and Dr. Maksym Zhukovskyi for his help with TEM imaging. The Graphical Abstract was prepared using Biorender.

Supplementary materials

Supplementary material associated with this article can be found, in the online version, at doi:10.1016/j.actbio.2020.12.033.

References

[1] M. Heron, Deaths: leading causes for, National Vital Statisticz Reports 68 (2019) (2017) 77.
[2] H. Thomas, J. Diamond, A. Vieco, S. Chaudhuri, E. Shinnar, S. Cromer, P. Perel, G.A. Mensah, J. Narula, C.O. Johnson, G.A. Roth, A.E. Moran, Global atlas of cardiovascular disease 2000-2016: the path to prevention and control, Global Heart. 13 (2018) 143, doi:10.1016/j.gheart.2018.09.511.
[3] B. Gorenek, C. Blomström Lundqvist, J. Brugada Terradellas, A.J. Camm, G. Hindricks, K. Huber, P. Kirchhof, K.-.H. Kuck, G. Kudaiberdieva, T. Lin, A. Raviele, M. Santini, R.R. Tilz, M. Valgimigli, M.A. Vos, C. Vrints, U. Zeymer, S.B. Kristiansen, G.Y.H. Lip, T. Potpara, L. Fauchier, C. Sticherling, M. Roffi, P. Widimsky, J. Mehilli, M. Lettino, F. Schiele, P. Sinnaeve, G. Boriani, D. Lane, I. Savelieva, ESC Scientific Document Group, Cardiac arrhythmias in acute coronary syndromes: position paper from the joint EHRA, ACCA, and EAPCI task force, EP Europace 16 (2014) 1655–1673, doi:10.1093/europace/euu208.
[4] D.M. Henkel, B.J. Witt, B.J. Gersh, S.J. Jacobsen, S.A. Weston, R.A. Meverden, V.L. Roger, Ventricular arrhythmias after acute myocardial infarction: a 20-year community study, Am. Heart J. 151 (2006) 806–812, doi:10.1016/j.ahj.2005.05.015.
[5] M.J. Wilhelm, Long-term outcome following heart transplantation: current perspective, J. Thorac. Dis. 7 (2015) 549–551, doi:10.3978/j.issn.2072-1439.2015.01.46.
[6] J.A. Cowger, Addressing the Growing U.S. Donor Heart Shortage, J. Am. Coll. Cardiol. 69 (2017) 1715–1717, doi:10.1016/j.jacc.2017.02.010.
[7] E.J. Lee, D.E. Kim, E.U. Azeloglu, K.D. Costa, Engineered cardiac organoid chambers: toward a functional biological model ventricle, Tissue Eng. Part A 14 (2008) 215–225, doi:10.1089/tea.2007.0351.
[8] I.C. Turnbull, I. Karakikes, G.W. Serrao, P. Backeris, J. Lee, C. Xie, G. Senyei, R.E. Gordon, R.A. Li, F.G. Akar, R.J. Hajjar, J. Hulot, K.D. Costa, Advancing functional engineered cardiac tissues toward a preclinical model of human myocardium, FASEB j 28 (2014) 644–654, doi:10.1096/fj.13-228007.
[9] S. Fleischer, A. Shapira, O. Regev, N. Nseir, E. Zussman, T. Dvir, Albumin fiber scaffolds for engineering functional cardiac tissues, Biotechnol. Bioeng. 111 (2014) 1246–1257, doi:10.1002/bit.25185.
[10] S. Fleischer, A. Shapira, R. Feiner, T. Dvir, Modular assembly of thick multifunctional cardiac patches, Proc. Natl. Acad. Sci. USA. 114 (2017) 1898–1903, doi:10.1073/pnas.1615728114.
[11] D. Bejleri, B.W. Streeter, A.L.Y. Nachlas, M.E. Brown, R. Gaetani, K.L. Christman, M.E. Davis, A bioprinted cardiac patch composed of cardiac-specific extracellular matrix and progenitor cells for heart repair, Adv. Healthc. Mater. 7 (2018) 1800672, doi:10.1002/adhm.201800672.
[12] W.Y. Yeong, N. Sudarmadji, H.Y. Yu, C.K. Chua, K.F. Leong, S.S. Venkatraman, Y.C.F. Boey, L.P. Tan, Porous polycaprolactone scaffold for cardiac tissue engineering fabricated by selective laser sintering, Acta Biomater. 6 (2010) 2028–2034, doi:10.1016/j.actbio.2009.12.033.
[13] S. Pok, I.V. Stupin, C. Tsao, R.G. Pautler, Y. Gao, R.M. Nieto, Z.-.W. Tao, C.D. Fraser, A.V. Annapragada, J.G. Jacot, Full-thickness heart repair with an engineered multilayered myocardial patch in rat model, Adv. Healthc. Mater. 6 (2017) 1600549, doi:10.1002/adhm.201600549.
[14] M. Radisic, H. Park, F. Chen, J.E. Salazar-Lazzaro, Y. Wang, R. Dennis, R. Langer, L.E. Freed, G. Vunjak-Novakovic, Biomimetic approach to cardiac tissue engineering: oxygen carriers and channeled Scaffolds, Tissue Eng. 12 (2006) 2077–2091, doi:10.1089/ten.2006.12.2077.
[15] R.A. Neal, A. Jean, H. Park, P.B. Wu, J. Hsiao, G.C. Engelmayr, R. Langer, L.E. Freed, Three-dimensional elastomeric scaffolds designed with cardiac-mimetic structural and mechanical features, Tissue Eng. Part A 19 (2013) 793–807, doi:10.1089/ten.tea.2012.0330.
[16] S. Pok, F. Vitale, S.L. Eichmann, O.M. Benavides, M. Pasquali, J.G. Jacot, Biocompatible carbon nanotube–chitosan scaffold matching the electrical conductivity of the heart, ACS Nano 8 (2014) 9822–9832, doi:10.1021/nn503693h.
[17] B. Guo, P.X. Ma, Conducting polymers for tissue engineering, Biomacromolecules 19 (2018) 1764–1782, doi:10.1021/acs.biomac.8b00276.
[18] S.R. Shin, S.M. Jung, M. Zalabany, K. Kim, P. Zorlutuna, S. bok Kim, M. Nikkhah, M. Khabiry, M. Azize, J. Kong, K. Wan, T. Palacios, M.R. Dokmeci, H. Bae, X. (Shirley) Tang, A. Khademhosseini, Carbon-nanotube-embedded hydrogel sheets for engineering cardiac constructs and bioactuators, ACS Nano 7 (2013) 2369–2380, doi:10.1021/nn305559j.
[19] A.M. Martins, G. Eng, S.G. Caridade, J.F. Mano, R.L. Reis, G. Vunjak-Novakovic, Electrically conductive chitosan/carbon scaffolds for cardiac tissue engineering, Biomacromolecules 15 (2014) 635–643, doi:10.1021/bm401679q.

[20] J. Zhou, J. Chen, H. Sun, X. Qiu, Y. Mou, Z. Liu, Y. Zhao, X. Li, Y. Han, C. Duan, R. Tang, C. Wang, W. Zhong, J. Liu, Y. Luo, M. (Mengqiu) Xing, C. Wang, Engineering the heart: evaluation of conductive nanomaterials for improving implant integration and cardiac function, Sci. Rep. 4 (2015) 3733, doi:10.1038/srep03733.
[21] P. Hitscherich, A. Aphale, R. Gordan, R. Whitaker, P. Singh, L. Xie, P. Patra, E.J. Lee, Electroactive graphene composite scaffolds for cardiac tissue engineering: electroactive graphene composite scaffolds for cardiac tissue engineering, J. Biomed. Mater. Res. Part A 106 (2018) 2923–2933, doi:10.1002/jbm.a.36481.
[22] L. Zhao, A novel graphene oxide polymer gel platform for cardiac tissue engineering application, 3 Biotech 9 (2019) 401, doi:10.1007/s13205-019-1912-4.
[23] A. Navaei, N. Moore, R.T. Sullivan, D. Truong, R.Q. Migrino, M. Nikkhah, Electrically conductive hydrogel-based micro-topographies for the development of organized cardiac tissues, RSC Adv 7 (2017) 3302–3312, doi:10.1039/C6RA26279A.
[24] M. Malki, S. Fleischer, A. Shapira, T. Dvir, Gold Nanorod-Based Engineered Cardiac Patch for Suture-Free Engraftment by Near IR, Nano Lett 18 (2018) 4069–4073, doi:10.1021/acs.nanolett.7b04924.
[25] G. Ye, Z. Wen, F. Wen, X. Song, L. Wang, C. Li, Y. He, S. Prakash, X. Qiu, Mussel-inspired conductive Ti_2C-cryogel promotes functional maturation of cardiomyocytes and enhances repair of myocardial infarction, Theranostics 10 (2020) 2047–2066, doi:10.7150/thno.38876.
[26] F.T. Andón, B. Fadeel, Programmed cell death: molecular mechanisms and implications for safety assessment of nanomaterials, Acc. Chem. Res. 46 (2013) 733–742, doi:10.1021/ar300020b.
[27] S. Ye, Y. Jiang, H. Zhang, Y. Wang, Y. Wu, Z. Hou, Q. Zhang, Multi-walled carbon nanotubes induce apoptosis in RAW 264.7 cell-derived osteoclasts through mitochondria-mediated death pathway, J. Nanosci. Nanotechnol. 12 (2012) 2101–2112, doi:10.1166/jnn.2012.5677.
[28] C.S. Yah, The toxicity of Gold Nanoparticles in relation to their physiochemical properties., (2013). https://www.biomedres.info/abstract/the-toxicity-of-gold-nanoparticles-in-relation-to-their-physiochemicalrnproperties-1128.html (accessed April 8, 2020).
[29] S.R. Shin, Y.-C. Li, H.L. Jang, P. Khoshakhlagh, M. Akbari, A. Nasajpour, Y.S. Zhang, A. Tamayol, A. Khademhosseini, Graphene-based materials for tissue engineering, Adv. Drug Deliv. Rev. 105 (2016) 255–274, doi:10.1016/j.addr.2016.03.007.
[30] H. Lin, Y. Wang, S. Gao, Y. Chen, J. Shi, Theranostic 2D tantalum carbide (MXene), Adv. Mater. 30 (2018) 1703284, doi:10.1002/adma.201703284.
[31] B. Xu, M. Zhu, W. Zhang, X. Zhen, Z. Pei, Q. Xue, C. Zhi, P. Shi, Ultrathin MXene-micropattern-based field-effect transistor for probing neural activity, Adv. Mater. 28 (2016) 3333–3339, doi:10.1002/adma.201504657.
[32] K. Rasool, M. Helal, A. Ali, C.E. Ren, Y. Gogotsi, K.A. Mahmoud, Antibacterial activity of $Ti_3C_2T_x$ MXene, ACS Nano 10 (2016) 3674–3684, doi:10.1021/acsnano.6b00181.
[33] C. Dai, H. Lin, G. Xu, Z. Liu, R. Wu, Y. Chen, Biocompatible 2D titanium carbide (MXenes) composite nanosheets for pH-responsive MRI-guided tumor hyperthermia, Chem. Mater. 29 (2017) 8637–8652, doi:10.1021/acs.chemmater.7b02441.
[34] K. Rasool, K.A. Mahmoud, D.J. Johnson, M. Helal, G.R. Berdiyorov, Y. Gogotsi, Efficient antibacterial membrane based on two-dimensional Ti 3 C 2 T x (MXene) Nanosheets, Sci. Rep. 7 (2017) 1–11, doi:10.1038/s41598-017-01714-3.
[35] P. Thoniyot, M.J. Tan, A.A. Karim, D.J. Young, X.J. Loh, Nanoparticle–hydrogel composites: concept, design, and applications of these promising, multi-functional materials, Adv. Sci. 2 (2015) 1400010, doi:10.1002/advs.201400010.
[36] A. Rafieerad, W. Yan, G.L. Sequiera, N. Sareen, E. Abu-El-Rub, M. Moudgil, S. Dhingra, Application of Ti $_3$ C $_2$ MXene quantum dots for immunomodulation and regenerative medicine, Adv. Healthc. Mater. 8 (2019) 1900569, doi:10.1002/adhm.201900569.
[37] B.B. Murphy, P.J. Mulcahey, N. Driscoll, A.G. Richardson, G.T. Robbins, N.V. Apollo, K. Maleski, T.H. Lucas, Y. Gogotsi, T. Dillingham, F. Vitale, A gel-free $Ti_3C_2T_x$-based electrode array for high-density, high-resolution surface electromyography, Adv. Mater. Technol. 5 (2020) 2000325, doi:10.1002/admt.202000325.
[38] N. Driscoll, K. Maleski, A.G. Richardson, B. Murphy, B. Anasori, T.H. Lucas, Y. Gogotsi, F. Vitale, Fabrication of Ti_3C_2 MXene microelectrode arrays for in vivo neural recording, J. Visualized Exp. (2020), doi:10.3791/60741.
[39] Y.-Z. Zhang, K.H. Lee, D.H. Anjum, R. Sougrat, Q. Jiang, H. Kim, H.N. Alshareef, MXenes stretch hydrogel sensor performance to new limits, Sci. Adv. 4 (2018) eaat0098, doi:10.1126/sciadv.aat0098.
[40] C. Xing, S. Chen, X. Liang, Q. Liu, M. Qu, Q. Zou, J. Li, H. Tan, L. Liu, D. Fan, H. Zhang, Two-dimensional MXene (Ti_3C_2)-integrated cellulose hydrogels: toward smart three-dimensional network nanoplatforms exhibiting light-induced swelling and bimodal photothermal/chemotherapy anticancer activity, ACS Appl. Mater. Interfaces. 10 (2018) 27631–27643, doi:10.1021/acsami.8b08314.
[41] S. Rohr, D.M. Schölly, A.G. Kléber, Patterned growth of neonatal rat heart cells in culture. morphological and electrophysiological characterization, Circ. Res. 68 (1991) 114–130, doi:10.1161/01.RES.68.1.114.
[42] N.A. Geisse, S.P. Sheehy, K.K. Parker, Control of myocyte remodeling in vitro with engineered substrates, In Vitro Cellular Dev. Biol. - Animal 45 (2009) 343–350, doi:10.1007/s11626-009-9182-9.
[43] A. Grosberg, P.-L. Kuo, C.-L. Guo, N.A. Geisse, M.-A. Bray, W.J. Adams, S.P. Sheehy, K.K. Parker, Self-organization of muscle cell structure and function, PLoS Comput. Biol. 7 (2011) e1001088, doi:10.1371/journal.pcbi.1001088.
[44] M.-A. Bray, S.P. Sheehy, K.K. Parker, Sarcomere alignment is regulated by myocyte shape, Cell Motil. Cytoskeleton 65 (2008) 641–651, doi:10.1002/cm.20290.
[45] A.W. Feinberg, P.W. Alford, H. Jin, C.M. Ripplinger, A.A. Werdich, S.P. Sheehy, A. Grosberg, K.K. Parker, Controlling the contractile strength of engineered cardiac muscle by hierarchal tissue architecture, Biomaterials 33 (2012) 5732–5741, doi:10.1016/j.biomaterials.2012.04.043.
[46] A. Agarwal, J.A. Goss, A. Cho, M.L. McCain, K.K. Parker, Microfluidic heart on a chip for higher throughput pharmacological studies, Lab Chip. 13 (2013) 3599, doi:10.1039/c3lc50350j.
[47] C. Chung, H. Bien, E.A. Sobie, V. Dasari, D. McKinnon, B. Rosati, E. Entcheva, Hypertrophic phenotype in cardiac cell assemblies solely by structural cues and ensuing self-organization, FASEB J. 25 (2011) 851–862, doi:10.1096/fj.10-168625.
[48] A.S.T. Smith, H. Yoo, H. Yi, E.H. Ahn, J.H. Lee, G. Shao, E. Nagornyak, M.A. Laflamme, C.E. Murry, D.-.H. Kim, Micro- and nano-patterned conductive graphene–PEG hybrid scaffolds for cardiac tissue engineering, Chem. Commun. 53 (2017) 7412–7415, doi:10.1039/C7CC01988B.
[49] J.H. Tsui, N.A. Ostrovsky-Snider, D.M.P. Yama, J.D. Donohue, J.S. Choi, R. Chavanachat, J.D. Larson, A.R. Murphy, D.-.H. Kim, Conductive silk–polypyrrole composite scaffolds with bioinspired nanotopographic cues for cardiac tissue engineering, J. Mater. Chem. B. 6 (2018) 7185–7196, doi:10.1039/C8TB01116H.
[50] T. Hu, Y. Wu, X. Zhao, L. Wang, L. Bi, P.X. Ma, B. Guo, Micropatterned, electroactive, and biodegradable poly(glycerol sebacate)-aniline trimer elastomer for cardiac tissue engineering, Chem. Eng. J. 366 (2019) 208–222, doi:10.1016/j.cej.2019.02.072.
[51] N.J. Wilkinson, M.A.A. Smith, R.W. Kay, R.A. Harris, A review of aerosol jet printing—A non-traditional hybrid process for micro-manufacturing, Int. J. Adv. Manuf. Technol. 105 (2019) 4599–4619, doi:10.1007/s00170-019-03438-2.
[52] X. Lian, J. Zhang, S.M. Azarin, K. Zhu, L.B. Hazeltine, X. Bao, C. Hsiao, T.J. Kamp, S.P. Palecek, Directed cardiomyocyte differentiation from human pluripotent stem cells by modulating Wnt/β-catenin signaling under fully defined conditions, Nat. Protoc. 8 (2013) 162–175, doi:10.1038/nprot.2012.150.
[53] A. Acun, P. Zorlutuna, Engineered myocardium model to study the roles of HIF-1α and HIF1A-AS1 in paracrine-only signaling under pathological level oxidative stress, Acta Biomater. 58 (2017) 323–336, doi:10.1016/j.actbio.2017.06.023.
[54] B.W. Ellis, A. Acun, U.I. Can, P. Zorlutuna, Human iPSC-derived myocardium-on-chip with capillary-like flow for personalized medicine, Biomicrofluidics 11 (2017) 024105, doi:10.1063/1.4978468.
[55] M. Kapnisi, C. Mansfield, C. Marijon, A.G. Guex, F. Perbellini, I. Bardi, E.J. Humphrey, J.L. Puetzer, D. Mawad, D.C. Koutsogeorgis, D.J. Stuckey, C.M. Terracciano, S.E. Harding, M.M. Stevens, Auxetic cardiac patches with tunable mechanical and conductive properties toward treating myocardial infarction, Adv. Funct. Mater. 28 (2018) 1800618, doi:10.1002/adfm.201800618.
[56] Y. Ebrahim, M. Ahmed, W. Abdelsalam, S.-.C. Chau, Shape representation and description using the Hilbert curve, Pattern Recognit. Lett. 30 (2009) 348–358, doi:10.1016/j.patrec.2008.09.013.
[57] A. Navaei, H. Saini, W. Christenson, R.T. Sullivan, R. Ros, M. Nikkhah, Gold nanorod-incorporated gelatin-based conductive hydrogels for engineering cardiac tissue constructs, Acta Biomater. 41 (2016) 133–146, doi:10.1016/j.actbio.2016.05.027.
[58] W. Kim, C.H. Jang, G.H. Kim, A myoblast-laden collagen bioink with fully aligned Au nanowires for muscle-tissue regeneration, Nano Lett. 19 (2019) 8612–8620, doi:10.1021/acs.nanolett.9b03182.
[59] H. Rastin, B. Zhang, A. Mazinani, K. Hassan, J. Bi, T.T. Tung, D. Losic, 3D bioprinting of cell-laden electroconductive MXene nanocomposite bioinks, Nanoscale 12 (2020) 16069–16080, doi:10.1039/D0NR02581J.
[60] T. Vladkova, N. Krasteva, A. Kostadinova, G. Altankov, Preparation of PEG-coated surfaces and a study for their interaction with living cells, J. Biomater. Sci. Polymer Edition 10 (1999) 609–620, doi:10.1163/156856299X00838.
[61] G.K. Nasrallah, M. Al-Asmakh, K. Rasool, K.A. Mahmoud, Ecotoxicological assessment of $Ti_3C_2T_x$ (MXene) using a zebrafish embryo model, Environ. Sci.: Nano. 5 (2018) 1002–1011, doi:10.1039/C7EN01239J.
[62] N. Driscoll, A.G. Richardson, K. Maleski, B. Anasori, O. Adewole, P. Lelyukh, L. Escobedo, D.K. Cullen, T.H. Lucas, Y. Gogotsi, F. Vitale, Two-dimensional Ti_3C_2 MXene for high-resolution neural interfaces, ACS Nano. 12 (2018) 10419–10429, doi:10.1021/acsnano.8b06014.
[63] J.-.O. You, M. Rafat, G.J.C. Ye, D.T. Auguste, Nanoengineering the heart: conductive scaffolds enhance connexin 43 expression, Nano Lett. 11 (2011) 3643–3648, doi:10.1021/nl201514a.
[64] T. Dvir, B.P. Timko, M.D. Brigham, S.R. Naik, S.S. Karajanagi, O. Levy, H. Jin, K.K. Parker, R. Langer, D.S. Kohane, Nanowired three-dimensional cardiac patches, Nature Nanotech. 6 (2011) 720–725, doi:10.1038/nnano.2011.160.
[65] M. Parchehbaf-Kashani, M. Sepantafar, M. Talkhabi, F.A. Sayahpour, H. Baharvand, S. Pahlavan, S. Rajabi, Design and characterization of an electroconductive scaffold for cardiomyocytes based biomedical assays, Mater. Sci. Eng.: C 109 (2020) 110603, doi:10.1016/j.msec.2019.110603.
[66] S.D. Lundy, W.-.Z. Zhu, M. Regnier, M.A. Laflamme, Structural and functional maturation of cardiomyocytes derived from human pluripotent stem cells, Stem Cells Dev. 22 (2013) 1991–2002, doi:10.1089/scd.2012.0490.
[67] A.W. Feinberg, C.M. Ripplinger, P. van der Meer, S.P. Sheehy, I. Domian, K.R. Chien, K.K. Parker, Functional differences in engineered myocardium from embryonic stem cell-derived versus neonatal cardiomyocytes, Stem Cell Reports 1 (2013) 387–396, doi:10.1016/j.stemcr.2013.10.004.

[68] T.P. Dias, S.N. Pinto, J.I. Santos, T.G. Fernandes, F. Fernandes, M.M. Diogo, M. Prieto, J.M.S. Cabral, Biophysical study of human induced Pluripotent Stem Cell-Derived cardiomyocyte structural maturation during long-term culture, Biochem. Biophys. Res. Commun. 499 (2018) 611–617, doi:10.1016/j.bbrc.2018.03.198.
[69] J.G. Jacot, A.D. McCulloch, J.H. Omens, Substrate stiffness affects the functional maturation of neonatal rat ventricular myocytes, Biophys. J. 95 (2008) 3479–3487, doi:10.1529/biophysj.107.124545.
[70] A. Seal, A.K. Dalui, M. Banerjee, A.K. Mukhopadhyay, K.K. Phani, Mechanical properties of very thin cover slip glass disk, Bull. Mater. Sci. 24 (2001) 151–155, doi:10.1007/BF02710092.
[71] J.G. Jacot, J.C. Martin, D.L. Hunt, Mechanobiology of cardiomyocyte development, J. Biomech. 43 (2010) 93, doi:10.1016/j.jbiomech.2009.09.014.
[72] A. Acun, T.D. Nguyen, P. Zorlutuna, In vitro aged, hiPSC-origin engineered heart tissue models with age-dependent functional deterioration to study myocardial infarction, Acta Biomater. 94 (2019) 372–391, doi:10.1016/j.actbio.2019.05.064.
[73] A.J.S. Ribeiro, Y.-.S. Ang, J.-.D. Fu, R.N. Rivas, T.M.A. Mohamed, G.C. Higgs, D. Srivastava, B.L. Pruitt, Contractility of single cardiomyocytes differentiated from pluripotent stem cells depends on physiological shape and substrate stiffness, Proc. Natl. Acad. Sci. 112 (2015) 12705–12710, doi:10.1073/pnas.1508073112.
[74] Guo Yuxuan, Pu William T., Cardiomyocyte Maturation, Circ. Res. 126 (2020) 1086–1106, doi:10.1161/CIRCRESAHA.119.315862.
[75] P.P.S.S. Abadi, J.C. Garbern, S. Behzadi, M.J. Hill, J.S. Tresback, T. Heydari, M.R. Ejtehadi, N. Ahmed, E. Copley, H. Aghaverdi, R.T. Lee, O.C. Farokhzad, M. Mahmoudi, Engineering of mature human induced pluripotent stem cell-derived cardiomyocytes using substrates with multiscale topography, Adv. Funct. Mater. 28 (2018) 1707378, doi:10.1002/adfm.201707378.
[76] Ruan Jia-Ling, Tulloch Nathaniel L., V. Razumova Maria, Saiget Mark, Muskheli Veronica, Pabon Lil, Reinecke Hans, Regnier Michael, E. Murry Charles, Mechanical stress conditioning and electrical stimulation promote contractility and force maturation of induced pluripotent stem cell-derived human cardiac tissue, Circulation 134 (2016) 1557–1567, doi:10.1161/CIRCULATIONAHA.114.014998.
[77] J. Wang, C. Cui, H. Nan, Y. Yu, Y. Xiao, E. Poon, G. Yang, X. Wang, C. Wang, L. Li, K.R. Boheler, X. Ma, X. Cheng, Z. Ni, M. Chen, Graphene sheet-induced global maturation of cardiomyocytes derived from human induced pluripotent stem cells, ACS Appl. Mater. Interfaces 9 (2017) 25929–25940, doi:10.1021/acsami.7b08777.
[78] H. Zhu, K.S. Scharnhorst, A.Z. Stieg, J.K. Gimzewski, I. Minami, N. Nakatsuji, H. Nakano, A. Nakano, Two dimensional electrophysiological characterization of human pluripotent stem cell-derived cardiomyocyte system, Sci. Rep. 7 (2017), doi:10.1038/srep43210.